sustainability

MDPI

Article

Size Effect of Shear Strength of Recycled Concrete Beam without Web Reinforcement: Testing and Explicit Finite Element Simulation

Wei Wang [1,2], Xin Zeng [1], Emery Niyonzima [1], Yue-Qing Gao [1,*], Qiu-Wei Yang [3] and Shao-Qing Chen [4]

[1] College of Civil Engineering, Shaoxing University, Shaoxing 312000, China; wangwei1210@189.cn (W.W.); zx572761328@126.com (X.Z.); niyonzimaemery8@gmail.com (E.N.)
[2] Key Laboratory of Rock Mechanics and Geohazards of Zhejiang Province, Shaoxing University, Shaoxing 312000, China
[3] School of Civil and Transportation Engineering, Ningbo University of Technology, Ningbo 315211, China; yangqiuwei79@126.com
[4] State Grid Sichuan Electric Power Research Institute, Chengdu 610000, China; lizeshen@163.com
* Correspondence: gaoyueqing@usx.edu.cn

Abstract: Recycled concrete is a form of low-carbon concrete with great importance. The explicit finite element method is an economical and feasible method for analyzing static concrete structures, such as those made of recycled concrete. The shear strength of regular concrete beams has size effects. In this study, a group of physical tests on the size effect of the shear strength of recycled concrete beams without web reinforcement was carried out under the condition of a constant shear span ratio. The research results show that the shear strength of the test beam generally decreases with the increase in beam section height, and a regression formula of the shear strength was obtained, which can formulate this effect. The rationale and feasibility of the explicit finite element method solving the ultimate load of concrete structures (which can derive the shear strength) were briefly demonstrated, and an explicit finite element simulation of test beams was carried out. Results showed an obvious and phenomenologically regular size effect of the shear strength of recycled concrete beams without web reinforcement, which can be simulated by the explicit finite element method. This research aims to promote the study of low-carbon recycled concrete structures to a certain extent and encourage the application of economic explicit finite element methods for the static analysis of concrete structures.

Keywords: structural engineering; static analysis; test; explicit finite element method; low-carbon; recycled concrete beam; shear strength; size effect

Citation: Wang, W.; Zeng, X.; Niyonzima, E.; Gao, Y.-Q.; Yang, Q.-W.; Chen, S.-Q. Size Effect of Shear Strength of Recycled Concrete Beam without Web Reinforcement: Testing and Explicit Finite Element Simulation. *Sustainability* **2021**, *13*, 4294. https://doi.org/10.3390/su13084294

Academic Editors: Xiao Yong Wang and Marc A. Rosen

Received: 30 January 2021
Accepted: 23 March 2021
Published: 13 April 2021

1. Introduction

Recycled concrete is an important form of low-carbon-emission concrete; similarly, numerical simulation methods are generally regarded as low-carbon analysis methods compared with physical tests. The mass formed by waste concrete processing is commonly utilized as coarse aggregate, and the material formed by mixing it with inorganic binding substances, such as fine aggregate, cement, water, etc., is called recycled concrete (ReC) [1]. It is generally considered that ReC is a green, low-carbon-emission material, which has a certain positive role in the protection of resources and the environment [2]. It is worth noting that, from a broad perspective of processes in research, production and living, among multiple behaviors that can achieve the same goal, those producing lower greenhouse gas emissions are collectively called low-carbon behaviors [3]. Physical tests and numerical simulation tests are two common methods of studying building structures, and the finite element method is a regular means to carry out structural numerical simulation tests [4]. In most cases, the numerical simulation method is obviously a relatively low-carbon analysis method.

At present, recycled concrete material properties and the mechanical properties of components cast from ReC are research hotspots in civil engineering. Research on recycled concrete material properties mainly involves strength [5], carbonization performance [6], durability [7], and creep performance studies [8]. Studies on the mechanical properties of recycled concrete components mainly include the bending performance of the slab [9,10], the deformation performance [11], the compression performance [12] and the shearing performance [13] of the column, as well as the deformation performance [14], the bending performance [15] and the shearing performance [16–22] of the beam. In actual engineering, the main failure mode of concrete beams is shear failure. In order to make the beam meet the ultimate bearing capacity requirements, it is necessary to calculate the shear resistance of the beam [23]. Therefore, studies on the shear resistance of recycled concrete beams are of great significance.

From an engineering point of view, the shear resistance of concrete beams includes the itemized shear resistance of web reinforcement and the itemized shear resistance of concrete [24], and the latter is quantitatively affected by material characteristics. One of the inherent characteristics of recycled concrete, which is a quasi-brittle material, is the size effect [25], that is, the mechanical properties of a certain material depend on the specific geometric dimensions of the solid object made from it. In addition, it can be inferred that there is a size effect on the itemized shear resistance of concrete that makes up the overall shear resistance of recycled concrete beams. Hereinafter, the concrete itemized shear resistance of recycled concrete beams will be referred to as SRRC. A number of studies on the overall shear resistance of recycled concrete beams exist [16–21], as well as reports on the size effect of the concrete itemized shear resistance of original concrete beams [26–31]. However, research on the size effect of SRRC has been limited, with only one report by Zhao et al. found in the literature [22]. Although it is an experimental study on the size effect of SRRC under the condition of a constant shear span ratio, it provides only qualitative assessment and lacks the quantification of this effect. Besides, it does not use the finite element method for supplementary parameter analysis for limited experimental data. Therefore, it is necessary to carry out further physical tests on the size effect of the concrete itemized shear resistance (or SRRC) of recycled concrete beams.

The finite element method is a universal and economical numerical parameter analysis method for solving structural static problems in solid mechanics. If it is used reasonably and scientifically, it will assist with the study of the SRRC size effect. The essence of the finite element method is translating the solving of the problem of continuum mechanics described by a differential equation, into the solving of an approximately equivalent system of algebraic equations [32]. Compared with the physical test method, the finite element method can carry out structural analysis at a lower cost [33]. Obviously, this advantage is conducive to carrying out structural parameter analysis, which is an important method for reaching a comprehensive description of the characteristics of the research object [34]. R. Tartaglia et al. used the finite element parameter analysis method to study the internal force in the flange of the T-stub, the change law of the internal force in the bolt rod, the distance from the bolt hole to the flange edge, and flange bending and other manufacturing defects that influence the mechanical behavior of the profile [35].

In finite element static analysis of concrete structures, the system of algebraic equations to be solved is nonlinear. At present, implicit and explicit algorithms are commonly used to solve the incremental form of this system [36]. Since the damage constitutive model can better describe the mechanical behavior of concrete materials, such as the mechanical phenomenon of strain-softening when concrete is cracked or crushed [37], it is often used when constructing concrete structure models [38]. In the above case, the algebraic systems describing the equilibrium are nonlinear. The static incremental step strategy is commonly used to approximate the equilibrium path [32]. At present, the algorithms for solving incremental steps mainly include implicit algorithms (the so-called Newton-like algorithms) and explicit algorithms [39]. The essence of an implicit algorithm is to use a kind of iterative method to directly solve the algebraic system of static balance described

in the incremental form [40]. The implicit algorithm is often recommended as a general method to solve nonlinear problems in commercial finite element software [41]. One of its limitations is that, when solving structural static problems with local instability phenomena (such as cracking when concrete structures are forced), it is generally difficult to obtain a convergent solution [42]. For concrete beams, when the external load has approached the peak load of SRRC [23], inclined cracks have already appeared in the shear area of the concrete beam. From the foregoing of two points, it is easy to infer that it is difficult for the implicit algorithm to research the SRRC size effect. The essence of the explicit algorithm is to convert the static problem of the original structure into the corresponding structural dynamic problem, perform a pseudo-static analysis on this problem, and approximate the result of the pseudo-static analysis as the solution to the original static problem [43]. The static problem that the explicit algorithm can approximately solve does not depend on the material, geometry, and continuity characteristics of the problem at all [44]. To date, there have been many reports on the use of explicit algorithms to carry out approximate static analysis of concrete structures [45–47]. For example, Yao et al. [46] used an explicit finite element method to analyze the four-point bending beam of concrete in order to verify the reliability of the explicit algorithm in solving the quasi-static response of concrete beams. There is good agreement with the test results. Yu et al. [47] used the arch effect to explain the shear mechanism of variable cross-section beams, conducted finite element analysis on four cantilever beams without web reinforcement, proposed the influence coefficient of the compression inclination on the arch effect and the method to determine the position of the check section, and established the relationship between the standard formula for shear resistance and the formula for calculating the shear resistance of beams with variable cross-sections. However, no study exists on the use of explicit algorithms to investigate the size effect of SRRC. Therefore, the present study aims to use the explicit finite element method to carry out simulation experiments on the SRRC size effect.

In summary, the main contribution of this work is the testing and explicit finite element simulation of the shear strength of a group of recycled concrete beams without web reinforcement under the condition of a constant shear span ratio.

The purpose of this paper is to report that SRRC (the concrete itemized shear resistance of recycled concrete beams) has a size effect, and this effect can be simulated by the explicit finite element method but is difficult to simulate using the implicit finite element method.

The paper is structured as follows. An overview of the physical tests is provided in Section 2, including the specimen design, the loading equipment, and the loading system. In Section 3, an overview of the simulation tests is given, including the physical discrete and contact settings, material constitutive model selection, loading system, and solution algorithm. In Section 4, some typical test results and related discussions are provided first. Next, a regression formula is presented, which can reflect the size effect of shear strength. Section 5 concludes this paper.

2. Overview of Physical Tests

2.1. Specimen Design

A total of four recycled concrete beams numbered B120, B180, B240, and B300 were designed and poured with the same batch of recycled concrete. Before pouring the 4 test specimens, the test materials and test mix ratios need to be determined. They are introduced as follows [22].

Firstly, the test materials include natural fine aggregate, recycled coarse aggregate and cement.

In this study, the performance indicators for natural fine aggregate are presented in Table 1.

Table 1. Parameters of fine aggregate.

Fine Aggregate	Particle Size/mm	Apparent Density/(kg/m^3)	Bulk Density/(kg/m^3)	Moisture Content/%	Fineness Modulus Number/μf	Water Absorption/%
Yellow sand	<5	2548	1211	6.8	1.83	2.9

When determining the recycled coarse aggregate, certain factors are also mainly taken into account, such as density, water absorption, moisture and size. For details of the performance indicators of the coarse recycled aggregate selected in this study, see Table 2.

Table 2. Parameters of recycled coarse aggregate.

Apparent Density/(kg/m^3)	Bulk Dense/(kg/m^3)	Water Absorption/%	Moisture Content/%	Crush Value Index/%	Porosity/%	Porosity/%	Pudding Rate/%
2481	1240	6.3	2.2	19.9	5.7	51.0	42.9

When determining the cement, some factors are mainly considered compressive, such as density. The cement used in this test is ordinary Portland cement with a strength level of 32.5. For some performance indicators of the cement selected in this study, see Table 3.

Table 3. Parameters of cement.

Density/(kg/m^3)	Compressive Strength/MPa		Flexural Strength/MPa	
	3d	28d	3d	28d
3051	17.8	35	3.9	7.1

Secondly, the mix ratio is designed. The ratio used to produce ReC, the strength level of which is C30, the slump is 70 mm, and which was used to cast the 4 beams tested in this study, is given by Table 4.

Table 4. Recycled concrete mix design.

Replacement Rate/%	Water-Cement Ratio	Material Consumption Per Cubic Meter/(kg/m^3)			
		Cement	Water	Sand	Recycled Coarse Aggregate
100	1:0.34	623.3	211.8	491.4	1073.5

After testing, the average uniaxial compressive strength of this recycled concrete was

$$\sigma_{cp} = 19.88 \text{ MPa}, \quad (1)$$

and the initial elastic modulus was

$$E_c = 2.588 \times 10^4 \text{ MPa}. \quad (2)$$

Based on the purpose of the test, the test beam was not equipped with stirrups. However, so that insufficient bending strength would not affect the results of the shear strength test, two longitudinal bars were arranged at the bottom of the beam. The position, yield strength (f_y), elastic modulus (E_s) and area (A_s) information of the longitudinal bars in each beam, and the size information of each beam, are shown in Figure 1 and Table 5. Only two supporting points of the test beam were located at the bottom of the beam, and the form was simply supported; the only concentrated force loading point was at the top of the beam. The specific positions of the supporting point and the loading point are shown in Figure 1 and Table 5. It is easily deduced that the beam's shear span ratio is $\lambda = l_2/h_0 = 2.45$, where l_2 is the horizontal distance between the supporting point and

the loading point, and h_0 is the effective height. After the estimation and according to the above-mentioned geometric dimensions, steel bar configuration, material strength and loading design, the failure mode of recycled concrete beams will be guaranteed to be shear failure, and thus the research purpose can be achieved.

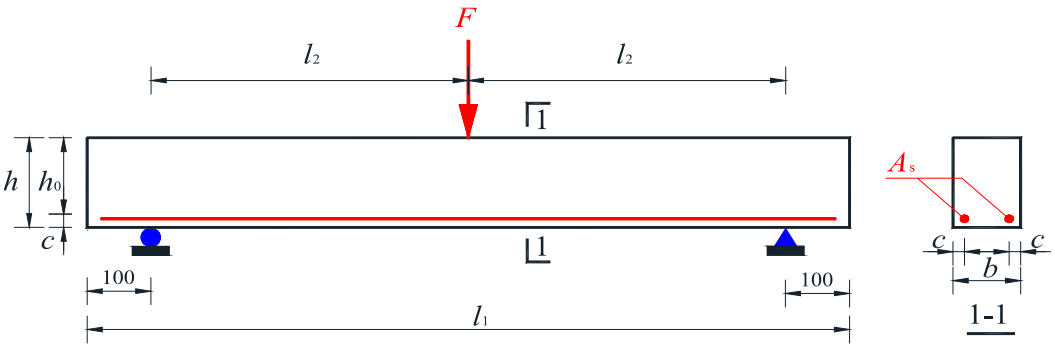

Figure 1. Geometrical properties of specimens.

Table 5. The dimensions of specimens and the properties of steel bars.

Specimen	l_1/mm	l_2/mm	b/mm	h/mm	h_0/mm	A_s/(mm^2)	f_y/MPa	E_s/MPa
B-120	740	270	120	120	110	157.00	481	1.96×10^5
B-180	1010	405	120	180	165	307.72	459	1.89×10^5
B-240	1280	540	120	240	220	401.92	421	2.12×10^5
B-300	1550	675	120	300	275	508.68	414	2.12×10^5

2.2. Loading Equipment and Loading System

The loading details of the test are depicted in Figure 2, where Figure 2a shows the reaction frame, and Figure 2b includes the details of the loading configuration. During loading, the preset loading schedule was implemented by simultaneously 'controlling the oil output rate of the oil pump to slowly move the jack lifting sleeve down, and monitoring the force value of the force indicator connected to the force sensor'.

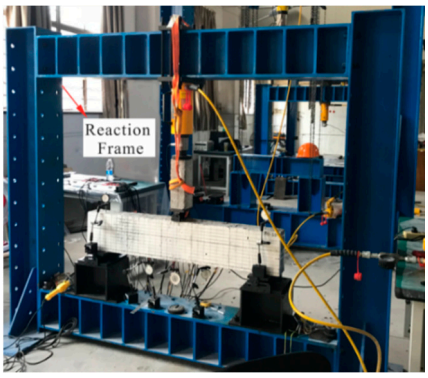

(**a**) Reaction frame

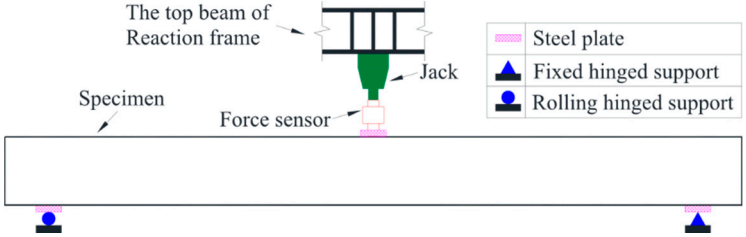

(**b**) Illustration of the test setup

Figure 2. Test setup.

The whole loading history was divided into two stages (pre-loading and formal loading) with different loading schedules. Before formal loading, preload was applied at about 50% of the estimated cracking load, $F_{cr,c} = M_{cr,c}/l_2$, where the cracking moment for the flexural load capacity of a normal section of beams without web reinforcement, $M_{cr,c}$, was calculated according to the formula given in the literature [24]:

$$M_{cr,c} = 0.292[1 + 5\times A_s E_s/(bhE_c)]\sigma_{tp}bh^2.$$

In the formula, σ_{tp} is the peak tensile stress, and based on the formula derived from literature [24] and literature [48],

$$\sigma_{tp} = 0.395 \times (\sigma_{cp}/0.715)^{0.55}. \quad (3)$$

After calculating, σ_{tp} equals to 2.46 MPa. The formal loading phase was divided into three subphases. Firstly, the increment of $\Delta F_1 \approx 0.1F_{cr,c}$ was used to increase the concentrated load F from 0 to the actual cracking load, $F_{cr,c}$. Secondly, $\Delta F_2 \approx 0.1(F_{q,c} - F_{cr,t})$ was applied to increase $F = F_{cr,t}$ approximately to $F_{q,c}$. The latter, $F_{q,c}$, is the quantile value of the estimated ultimate load ($F_{u,c}$) and in this study is equal to $0.7F_{u,c}$. This paper used the formula $V_{u,c} = 1.75\sigma_{tp}bh_0/(\lambda + 1)$ to estimate $F_{u,c} = 2V_{u,c}$, given by the literature [25] for the shear bearing capacity of the oblique section of beams without web reinforcement. Thirdly, $\Delta F_3 \approx 0.1(F_{u,c} - F_{q,c})$ was used to increase $F = F_{q,c}$ to the measured limit load, $F_{u,t}$. $M_{cr,c}$, $F_{cr,c}$, $F_{u,c}$, $F_{q,c}$, ΔF_1, ΔF_2, and ΔF_3 were calculated according to the above principles and $F_{cr,t}$, as seen in Table 6, thus determining the load control points during the entire test loading history.

Table 6. Several important estimated loads and internal forces.

Specimen ID	$M_{cr,c}$/(kN·m)	$F_{cr,c}$/kN	ΔF_1/kN	$F_{cr,t}$/kN	$F_{u,c}$/kN	$F_{q,c}$/kN	ΔF_2/kN	ΔF_3/kN
B-120	1.78	6.60	1.00	16.00	33.43	23.40	1.00	1.00
B-180	4.31	10.70	1.00	18.00	50.15	35.11	1.00	1.00
B-240	7.93	14.70	1.00	30.00	66.87	46.81	1.00	2.00
B-300	12.40	18.40	2.00	26.30	83.59	58.51	3.00	2.00

3. Overview of Simulation Test

3.1. Physical Discrete Setting and Contact Conditions

In this paper, Abaqus software was used to carry out the geometrical discrete and contact settings of the finite element model of the specimen. The operation mainly involved six aspects. Firstly, the element type was determined. Both the beam entities and the steel cushion blocks were discrete, with an eight-node reduced integral format three-dimensional entity element. The number for this element in the Abaqus element library is C3D8R. Reinforcing bars were discretized by three-dimensional two-node line elements, with the number T3D2. Secondly, the element size was determined. For the rectangular solid elements of discrete steel cushion blocks and beam entities, the three orthogonal edges on the surface were parallel to the three orthogonal edges on the beam surface (see Figure 3), and the dimension of x_l along the beam length was l_e, the dimension of the direction x_h along the beam height was h_e, and the dimension of x_b along the beam width was b_e. For the concrete element in the column of the cushion blocks, however, the dimension in the x_l direction was $l_{e,in}$; for the concrete element from the beam end to the supporting cushion block area, the dimension in the x_l direction was $l_{e,out}$. The dimensions of all the above physical elements are shown in Table 7. For the linear element of the discrete steel bars, the dimension l_{es} along the beam length direction x_l is also shown in Table 7, and its position in the plane x_b-x_l is shown in Figure 1. Thirdly, it was determined how steel and concrete interact. This article assumed that there was no bond-slip behavior between the steel bar and the concrete, and thus the 'Embedded' constraint was selected to embed the steel bar in the concrete entity. Fourthly, the contact mode between the steel

cushion block and the concrete entity was determined. Herein, the mechanical behaviors of the upper and lower neighborhoods of the contact surface between the cushion blocks and the beam are set as follows: the contact surface between the left and right supporting cushion block and the bottom of the beam, and the contact surface between the loading cushion block and the top of the beam, adopted the 'Tie' mode to combine into a continuous medium area. Fifthly, boundary conditions were identified. In order to better simulate actual working conditions, the lower surface of the left and right supporting cushion block only had rotational degrees of freedom around x_b and x_h. Sixthly, the constitutive response law of the neighboring concrete at the concentrated force was assumed. Extremely high stresses occur in concrete elements near the supporting/loading cushion blocks. In order to prevent these from exceeding the description range of the concrete damage constitutive model and subsequently causing calculation failures, the constitutive model of the steel cushion block was adopted for the concrete elements that are in contact with the left and right supporting cushion blocks and for the concrete element in contact with the loading cushion block (as shown in the red area in Figure 3). The mathematical expression of this model is shown in Section 3.2. According to the above six operational steps, a three-dimensional view of the finite element model of the beam, numbered B-120, is shown in Figure 3.

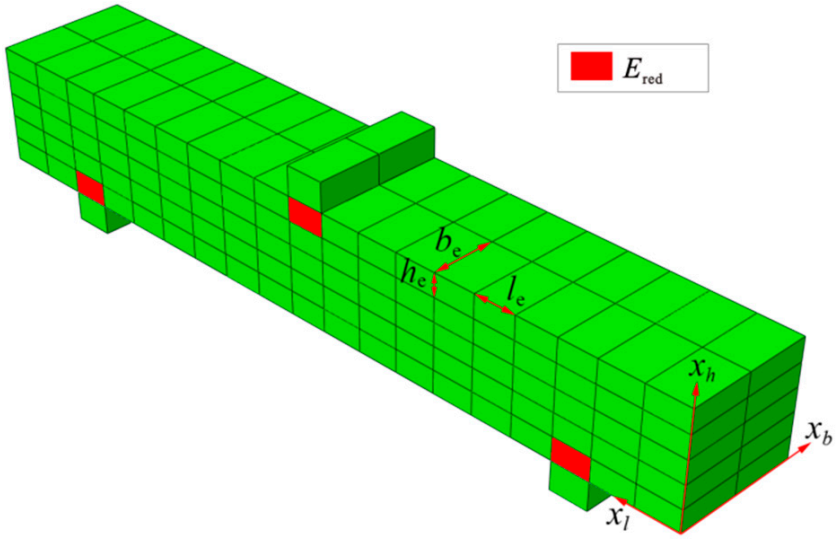

Figure 3. Finite element model of tested beam B-120. (Note: E_{red} is the concrete elements that used the constitutive model of the steel cushion block).

Table 7. Dimensions of each element in finite element models of specimens/mm.

Specimen ID	Concrete Element					Steel-Pad Element			Steel-Bar Element
	l_e/mm	$l_{e,in}$/mm	$l_{e,out}$/mm	h_e/mm	b_e/mm	l_e/mm	h_e/mm	b_e/mm	l_{es}/mm
B-120	39	36	41	24	60	36	30	60	40
B-180	50.6	50.5	74.8	30	60	50.5	30	60	51.6
B-240	48.9	51.2	74.4	40	60	51.2	30	60	49.6
B-300	61.3	60.2	69	50	60	62.0	30	60	62.5

3.2. Material Constitutive Model

Before static analysis, constitutive models of various components in the finite element discrete model need to be selected.

Firstly, the constitutive model of the steel cushion blocks was selected. According to the local influence principle [49], the selection of the constitutive model of the steel cushion block has a limited effect on the simulation results of the static behavior of the concrete

beam. Therefore, in static loading, it can be assumed that the steel pad is always in a linear elastic state. Therefore, this study selected a linear elastic constitutive model for the steel cushion block, which can be expressed as

$$\boldsymbol{\sigma} = \boldsymbol{D}^{\mathrm{e}} : \boldsymbol{\varepsilon},$$

where $\boldsymbol{\sigma}$ is the Cauchy stress, $\boldsymbol{\varepsilon}$ is the Cauchy strain tensor, and $\boldsymbol{D}^{\mathrm{e}}$ is the elastic stiffness tensor of the material, which is determined by the elastic modulus E_b and the Poisson's ratio ν_b of the steel cushion block [49]. In the simulation of this study, $E_b = 190$ GPa, and $\nu_b = 0.3$.

Secondly, the constitutive model of steel bars was selected. The simulated beam was a simply supported beam without web reinforcement. When it failed due to the insufficient shear strength of the oblique section, the longitudinal reinforcement had not yet generally entered the yield stage. Therefore, this study employed an ideal (one-dimensional) elastoplastic constitutive model for steel bars, which can be expressed as

$$\begin{cases} \sigma_{\mathrm{s}} = \mathrm{E_s}\varepsilon_{\mathrm{s}} & \varepsilon_{\mathrm{s}} < \varepsilon_{\mathrm{sy}} \\ \sigma_{\mathrm{s}} = f_{\mathrm{sy}} & \varepsilon_{\mathrm{s}} \geq \varepsilon_{\mathrm{sy}} \end{cases},$$

where σ_{s} and ε_{s} indicate stress scalar and strain scalar, respectively; and $\varepsilon_{\mathrm{sy}} = f_{\mathrm{y}}/E_{\mathrm{s}}$ is the initial yield strain, where f_{y} stands for the yield strength. In the simulation, the E_{s} and f_{y} of the longitudinal reinforcement in each simulated beam adopt the actual measured values of the longitudinal reinforcement in the corresponding test beam; see Table 5 for details.

Thirdly, the recycled concrete constitutive model was chosen. ① In the static test, there is a cracking phenomenon in the concrete, strain softening in the cracked area, and elastic-plastic strain unloading in the adjacent cracked area. Accordingly, this paper used the concrete damage plasticity (hereinafter referred to as CDP) constitutive model proposed by J. Lee et al. [50] for recycled concrete, which can describe the above behaviors and can be expressed as

$$\boldsymbol{\sigma} = (1-d)\boldsymbol{D}^{\mathrm{e}} : (\boldsymbol{\varepsilon} - \boldsymbol{\varepsilon}^{\mathrm{p}}), \tag{4}$$

where d is the damage variable (scalar) and $\boldsymbol{\varepsilon}^{\mathrm{p}}$ is the plastic strain tensor. According to this constitutive model theory [51,52], in the analysis, the stress-strain curve under the uniaxial (tension or compression) condition, the equivalent compression plastic strain $\tilde{\varepsilon}_{\mathrm{c}}^{\mathrm{p}}$, and the equivalent tension plastic strain $\tilde{\varepsilon}_{\mathrm{t}}^{\mathrm{p}}$ should be given. With the aid of several conversion rules, Formula (4) can be utilized to calculate the constitutive state of the integration point in the element. ② The literature [53] has pointed out that the stress-strain curve shapes of recycled concrete and original concrete are highly similar. Therefore, this study applied the uniaxial compressive stress-strain curve of concrete, as proposed by Guo [54],

$$\begin{cases} \sigma_{\mathrm{c}} = \sigma_{\mathrm{cp}}\left[\alpha_{\mathrm{c}}\frac{\varepsilon_{\mathrm{c}}}{\varepsilon_{\mathrm{cp}}} + (3-2\alpha_{\mathrm{c}})\left(\frac{\varepsilon_{\mathrm{c}}}{\varepsilon_{\mathrm{cp}}}\right)^2 + (\alpha_{\mathrm{c}}-2)\left(\frac{\varepsilon_{\mathrm{c}}}{\varepsilon_{\mathrm{cp}}}\right)^3\right] & (\varepsilon_{\mathrm{c}} \leq \varepsilon_{\mathrm{cp}}) \\ \sigma_{\mathrm{c}} = \sigma_{\mathrm{cp}}\left(\frac{\varepsilon_{\mathrm{c}}}{\varepsilon_{\mathrm{cp}}}\right)/\left[\beta_{\mathrm{c}}\left(\frac{\varepsilon_{\mathrm{c}}}{\varepsilon_{\mathrm{cp}}}-1\right)^2 + \frac{\varepsilon_{\mathrm{c}}}{\varepsilon_{\mathrm{cp}}}\right] & (\varepsilon_{\mathrm{c}} > \varepsilon_{\mathrm{cp}}) \end{cases}, \tag{5}$$

and the uniaxial tensile stress-strain curve

$$\begin{cases} \sigma_{\mathrm{t}} = \sigma_{\mathrm{tp}}\left[\alpha_{\mathrm{t}}\frac{\varepsilon_{\mathrm{t}}}{\varepsilon_{\mathrm{tp}}} + \left(\frac{6-5\alpha_{\mathrm{t}}}{4}\right)\left(\frac{\varepsilon_{\mathrm{t}}}{\varepsilon_{\mathrm{tp}}}\right)^2 + \left(\frac{\alpha_{\mathrm{t}}-2}{4}\right)\left(\frac{\varepsilon_{\mathrm{t}}}{\varepsilon_{\mathrm{tp}}}\right)^6\right] & (\varepsilon_{\mathrm{t}} \leq \varepsilon_{\mathrm{tp}}) \\ \sigma_{\mathrm{t}} = \sigma_{\mathrm{tp}}\left(\frac{\varepsilon_{\mathrm{t}}}{\varepsilon_{\mathrm{tp}}}\right)/\left[\beta_{\mathrm{t}}\left(\frac{\varepsilon_{\mathrm{t}}}{\varepsilon_{\mathrm{tp}}}-1\right)^{\varphi_{\mathrm{t}}} + \frac{\varepsilon_{\mathrm{t}}}{\varepsilon_{\mathrm{tp}}}\right] & (\varepsilon_{\mathrm{t}} > \varepsilon_{\mathrm{tp}}) \end{cases} \tag{6}$$

to construct the basic data required for numerical implementation of the above damage constitutive model. In the above two formulas, σ_{c} and ε_{c} are the compressive stress and compressive strain, respectively; σ_{cp} is the peak compressive stress; $\varepsilon_{\mathrm{cp}}$ is the strain corresponding to σ_{cp}; σ_{t} and ε_{t} are the tensile stress and tensile strain, respectively; σ_{tp} is the peak tensile stress; $\varepsilon_{\mathrm{tp}}$ is the strain corresponding to σ_{tp}; and α_{c}, β_{c}, α_{t}, β_{t} and φ_{t}

are all coefficients calibrated by the tests. Based on the tested σ_{cp} (the value is shown in Formula (1)), first calculate σ_{tp} according to Formula (2), and then calculate ε_{tp} according to the formula $\varepsilon_{tp} = 65{\sigma_{tp}}^{0.54} \times 10^{-6}$ [54]. The values of these three data are listed in Table 8. At the same time, according to [53,54], the selected or calculated values of ε_{cp}, α_c, β_c, α_t, β_t and φ_t are also listed in Table 8. According to Formulas (5) and (6) and the parameters in Table 8, the stress-strain curve is presented in Figure 4. ③ As suggested by the literature [52], the formula

$$\begin{cases} \tilde{\varepsilon}_c^p = \gamma_c(\varepsilon_c - \sigma_c/E_c) \\ \tilde{\varepsilon}_t^p = \gamma_t(\varepsilon_t - \sigma_t/E_c) \end{cases}$$

is chosen to describe $\tilde{\varepsilon}_c^p$ and $\tilde{\varepsilon}_t^p$. In the formula, E_c is the initial elastic modulus of concrete (its value is shown in Formula (2)), and γ_c and γ_t are the coefficients calibrated by the experiment, empirically taking the values of $\gamma_c = 0.7$ and $\gamma_t = 0.1$, based on the literature [52].

Table 8. Parameters for the stress-strain curves in the concrete constitutive model.

σ_{cp}/MPa	ε_{cp}	σ_{tp}/MPa	ε_{tp}	α_c	β_c	α_t	β_t	φ_t
19.88	1.80×10^{-3}	2.46	1.06×10^{-4}	2.34	4.0	1.1	1.89	1.7

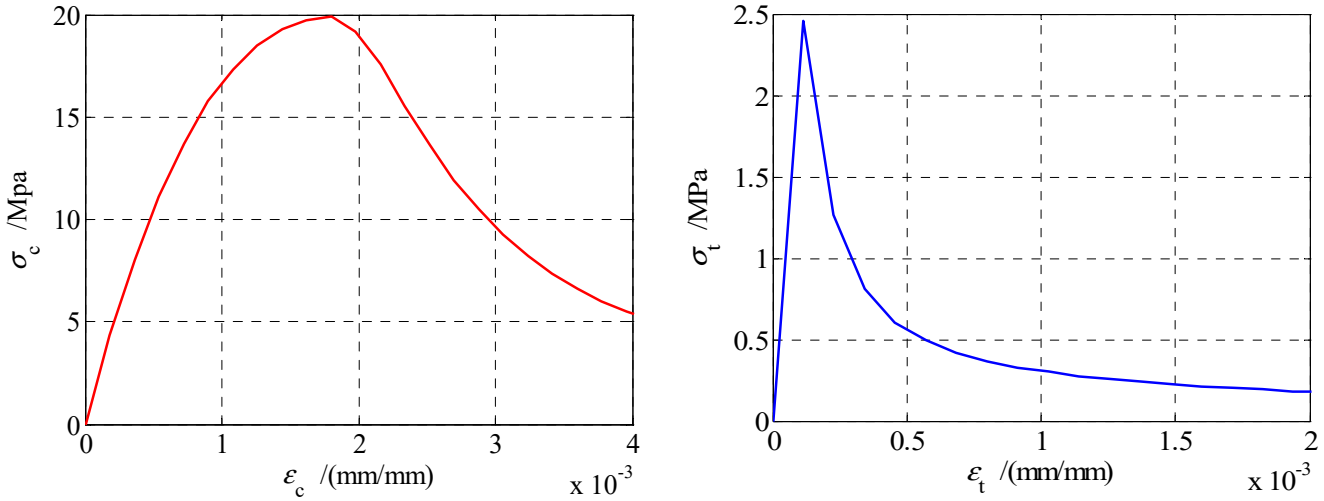

(**a**) Compression (**b**) Tension

Figure 4. σ-ε curves.

In order to increase the readability of the paper, follow the data input requirements of the CDP model in Abaqus. Four curves on the relationships of yield-stress (under compression) to inelastic-strain, compression-damage to inelastic-strain, yield-stress (under tension) to cracking-strain, and tension-damage to cracking-strain are shown in Figure 5.

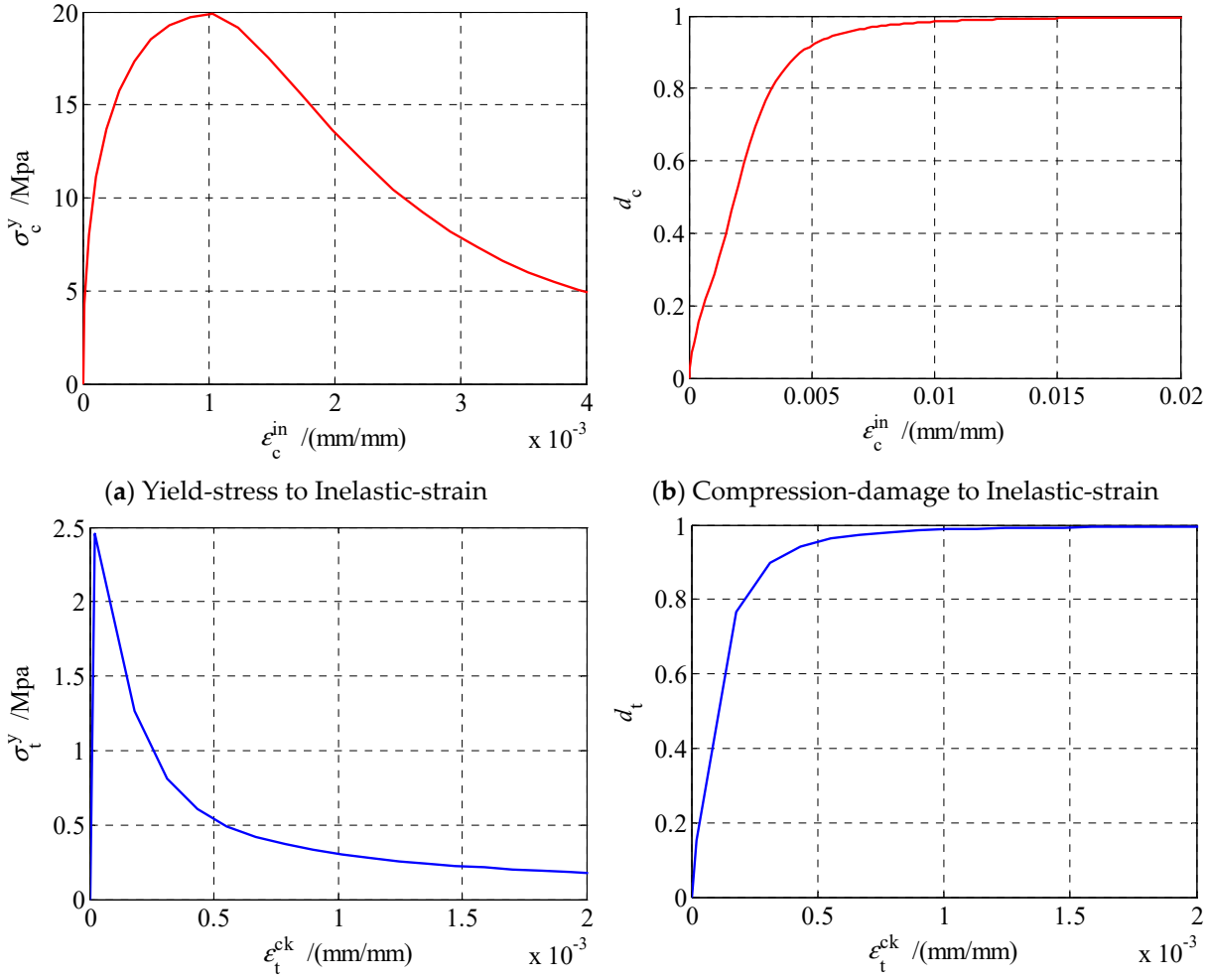

(**a**) Yield-stress to Inelastic-strain

(**b**) Compression-damage to Inelastic-strain

(**c**) Yield-stress to Cracking-strain

(**d**) Tension-damage to Cracking-strain

Figure 5. Data input requirements of the concrete damage plasticity (CDP) model in Abaqus. (Note: in the Figure, σ_c^y is yield-stress under compression, ε_c^{in} is inelastic-strain, d_c is compression-damage, σ_t^y is yield-stress under tension, ε_c^{in} is cracking-strain, and d_t is tension-damage).

3.3. Loading System and Solution Algorithm Configuration

Before performing the finite element simulation, it is also necessary to define the loading schedule and solving algorithm. In a similar way to the physical test, the displacement control loading mode is adopted in the simulation test, with a constant loading rate. The total loading time of each numerical beam model and the initial displacement/final displacement of the active loading point are shown in Table 9.

Table 9. Loading configuration.

Specimen ID	Total Loading time/s	Initial Loading Displacement/mm	Final Loading Displacement/mm	Displacement Changing Law
B-120	2	0.0	0.20	Linear
B-180	2	0.0	0.20	Linear
B-240	2	0.0	0.40	Linear
B-300	2	0.0	0.50	Linear

Configure the parameters of the implicit/explicit solver. For the implicit solver, the time period was set to 1, the loading point displacement changed linearly with time, the "Nlgeom" option was checked, the initial increment size was set to 0.001, the minimum

increment size was set to 1×10^{-5}, the maximum increment size was set to 0.01, and the iterative solution of the nonlinear equation system was Newton's method. For the explicit solver, the time period and the characteristics of loading point displacement in the time domain are shown in Table 9; check the "Automatic" option to determine the loading point increment, check the "Element-by-element" option to determine the stable increment step size, the time scaling factor was set to 1, the linear bulk viscosity parameter was set to 0.06, the quadratic bulk viscosity parameter was set to 1.2, and other parameters used the default values.

4. Results and Discussion

4.1. Failure Phenomenon and Characteristic Stress Contour Plots

The progress of crack development in the four beams was consistent with common sense, and the damage mode was typically uniform. When the load reached a certain level, normal transverse bending cracks first appeared in the area of maximum bending moment (mid-span). As the load increased, the area with normal bending cracks appearing enlarged, and the already existing normal bending cracks elongated. When the load continued to rise, shear oblique cracks appeared near the neutral axis of the beam, the oblique cracks extended to both ends, and part of the oblique cracks connected with the normal cracks. As the load reached an extreme value, a main diagonal crack suddenly appeared to tear the beam in a similar manner to the main control crack (the red curve) in beam B-240, as shown in Figure 6a, and the bearing capacity of the beam was lost. The progress diagram of the cracks (the curve in the figure) in beams B-120, B-180, and B-300 are shown in Figure 6b–d, respectively, in which the red curve refers to the main control crack. To determine the plane position of the cracks, an equidistant grid was drawn along the horizontal and vertical directions of the beam, and the grid number was marked with numbers and letters. The value near several positions of the crack represents the value of the applied load (unit: kN) corresponding to the crack developed to reach this point. The crack progress diagram of beam B-240 was consistent with the characteristics of the first three beams.

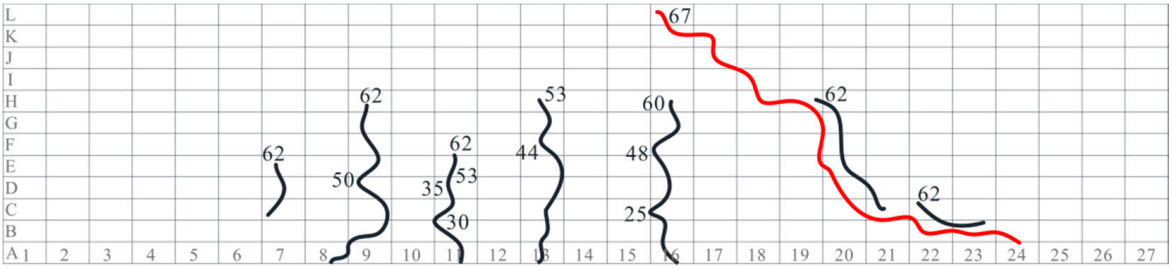

(**a**) B-240

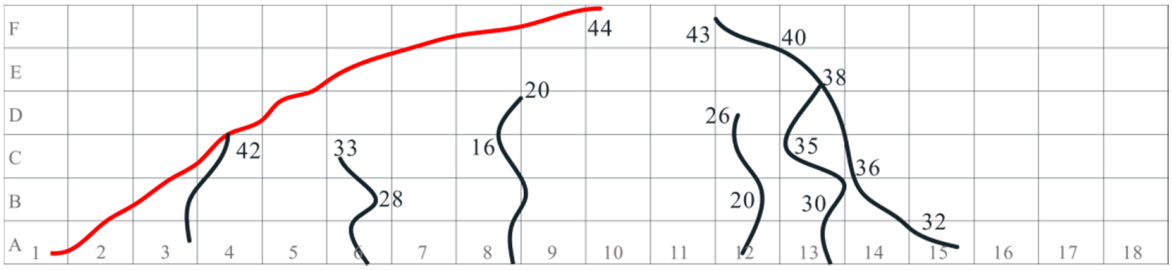

(**b**) B-120

Figure 6. *Cont.*

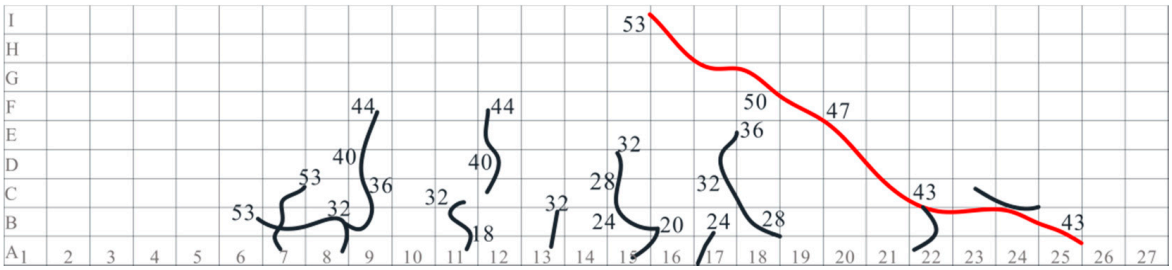

(**c**) B-180

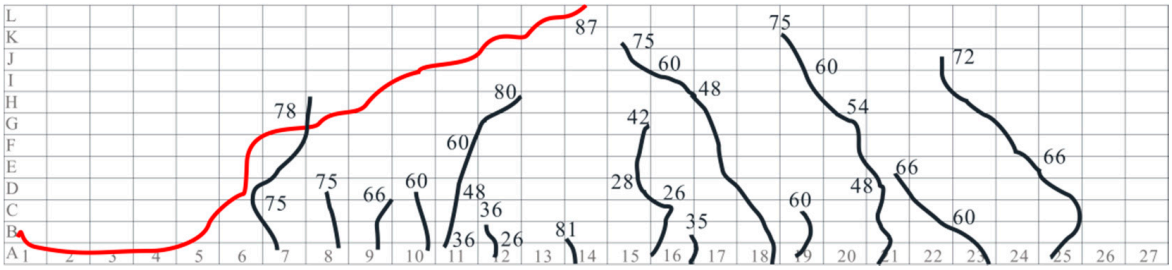

(**d**) B-300

Figure 6. The scenes of specimen cracking.

The typical stress contour plots provided by the finite element simulation can verify the aforementioned experimental phenomenon. The law of the main tension stress contour plots given by the finite element simulation was similar for all four beams, while this paper only selects the beam B-240 for analysis. In basic terms, Figure 7a shows the main tensile stress contour plot of the beam after removing the cushion blocks and the element immediately adjacent to the cushion blocks. From this figure, it is clear that there is a high principal tensile stress in the high-stress area near the cushion blocks and the high-bending effect area at the bottom of the mid-span beam, which is qualitatively consistent with the common sense of elasticity and material mechanics; the principal tensile stress in the vicinity of the neutral axis of the beam is substantial. This phenomenon can also be qualitatively described by the theory of material mechanics—the shear stress here is large, but the normal stress is zero. Subsequently, the distribution of the aforementioned shear stress peak area can also be described by the contour map of Tresca stress τ_{max}, as shown in Figure 7b ($\tau_{max} = (\sigma_1 - \sigma_3)/2$), where σ_1 and σ_3 are the maximum and minimum principal stresses, respectively. In particular, in the bending neutral axis area with high shear stress but low normal stress, the area with a large τ_{max} value will produce inclined cracks at an angle of 45 to the neutral axis, and this simulation results confirms the test results given in Figure 6.

In summary, crack development in the test is close to the result obtained by the simulation, and both belong to the shear failure mode.

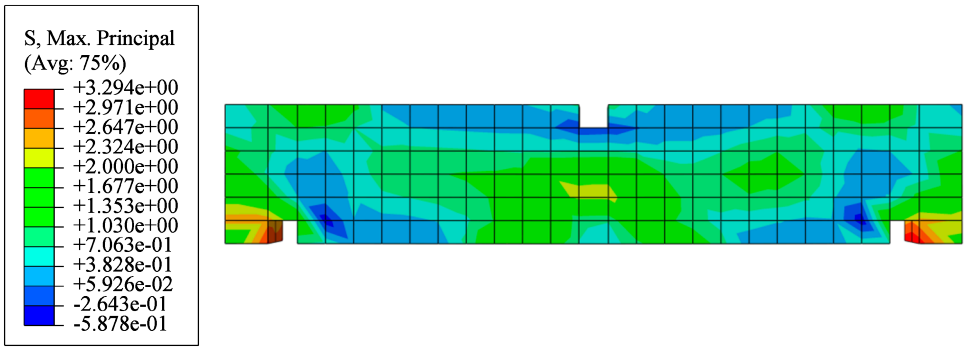

(**a**) Principal tensile stress contour plot of beam B-240

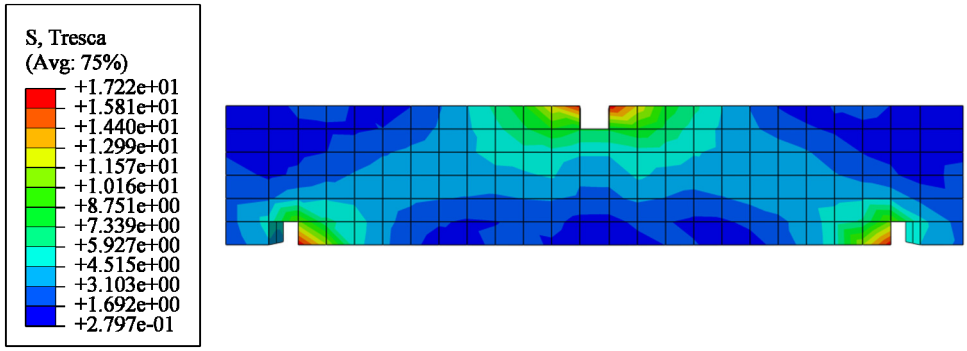

(**b**) Tresca stress contour plot of beam B-240

Figure 7. Characteristic stress contour plots.

4.2. Ultimate Load in Test and Simulation

The ultimate loads given by the simulation and experiment were very similar. Explicit and implicit algorithms were used to carry out the simulation analysis. The ultimate load $F^{\mathrm{e}}_{\mathrm{u,s}}$ was calculated by the explicit algorithm, and the ultimate load $F^{\mathrm{i}}_{\mathrm{u,s}}$ was calculated by the implicit algorithm, as shown in Table 10. In the table, the subscript t represents the test value, the subscript *s* indicates the simulated value, the superscript *e* represents the simulated value given by the explicit algorithm, and the superscript *i* denotes the simulated value given by the implicit algorithm. In combination with the ultimate load $F_{\mathrm{u,t}}$ given by the test, the relative error is $\varepsilon^{i}_{\mathrm{err}} = \left|F^{i}_{\mathrm{u,s}} - F_{\mathrm{u,t}}\right| / F_{\mathrm{u,t}}$ ($i = \mathrm{e}, \mathrm{i}$). Obviously, for each beam, $\varepsilon^{\mathrm{e}}_{\mathrm{err}}$ is not only small but also much smaller than $\varepsilon^{i}_{\mathrm{err}}$. This shows that the constitutive model used in this paper and the approximate solution algorithm of the selected nonlinear equations—the explicit algorithm—are reasonable. However, from the four sample points alone, there is clearly no qualitative relationship between $\varepsilon_{\mathrm{err}}$ and the height of the beam h (See Table 5).

Table 10. Numerical results for test and simulation.

Specimen ID	$F_{\mathrm{u,t}}$/kN	$F^{\mathrm{e}}_{\mathrm{u,s}}$/kN	$F^{\mathrm{i}}_{\mathrm{u,s}}$/kN	τ_{t}/MPa	$\tau^{\mathrm{e}}_{\mathrm{s}}$/MPa	$\tau^{\mathrm{i}}_{\mathrm{s}}$	$\varepsilon^{\mathrm{e}}_{\mathrm{err}}$	$\varepsilon^{\mathrm{i}}_{\mathrm{err}}$
B-120	44.00	47.06	30.96	1.67	1.78	1.17	6.95%	29.64%
B-180	53.00	53.49	56.30	1.34	1.35	1.42	0.92%	6.23%
B-240	67.00	70.88	29.80	1.27	1.34	0.56	5.79%	55.52%
B-300	87.00	86.07	54.78	1.32	1.30	0.83	1.13%	37.03%

4.3. Law of Shear Strength and Its Value

Shear strength can be easily calculated based on the test and simulation results provided in the previous section. In concrete structure engineering, the shear strength of concrete beams is generally determined by the formula $\tau = V_{\mathrm{u}}/bh_0$ [55], where b is the

beam width and h_0 is the effective height of the cross-section of the beam—the two values for each specimen are shown in Table 5—and V_u represents the ultimate shear bearing capacity of the cross-section. According to Figure 1, $V_u = F_u/2$, where F_u is the ultimate load given by test or simulation (see Table 10 for specific values). According to the above, the calculated shear strength τ values are shown in Table 10.

The values of shear strength τ_t given by the test show an obvious size effect phenomenon. This phenomenon not only has regression statistical characteristics but can also be confirmed by the explicit simulation results, $\tau_{s,e}$. The τ_t (dependent variable), with h_0 as the independent variable under the constant shear span ratio ($\lambda = 2.45$) given by the experiment, is shown in Figure 8. Based on the set of discrete data points (h_0, τ_t), the regression formula for describing the size effect is

$$\tau_t = 3.212 \times 10^9 \times h_0^{-4.856} + 1.279.$$

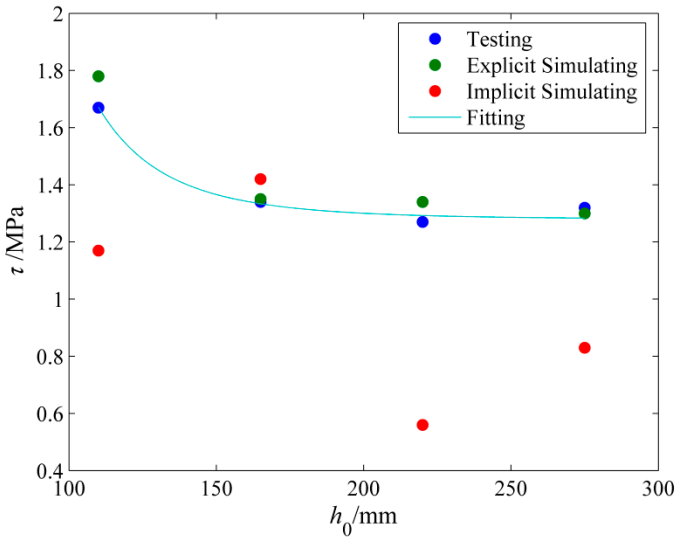

Figure 8. The test data of τ and its fitting curve.

The continuous curve of h_0 and τ_t obtained by the regression formula is shown in Figure 8; it is clearly seen that the fitting effect is qualitatively better. Either from the discrete data point set or from the fitting curve, it can be established that τ_t and h_0 are in a monotonous and nonlinear inverse proportional relationship: as h_0 increases, the deceleration rate of τ_t declines and shows a trend toward zero. Based on Table 10, the explicit simulation results are better than the implicit simulation results. The discrete data point set (h_0, $\tau_{s,e}$) given by the explicit simulation is shown in Figure 8. From the figure, it is easily derived that the law of explicit simulation data is the same as that of experimental discrete data, especially when h_0 is large. Herein, it is considered that this phenomenon has a certain scientific nature. As it is widely known, the accuracy of the approximate solution to the mathematical and physical problems (in this paper, the solid static problem) given by the structural finite element mainly depends on two factors: the ability to accurately describe the boundary conditions and the ability to accurately describe the general law of object behavior. Therefore, the explicit solution method provides a satisfactory solution for the finite element calculation of the shear strength of concrete beams described by the damage constitutive model.

5. Conclusions

In this paper, physical and simulation tests on the size effect of the shear strength of a group of recycled concrete beams without web reinforcement under the condition of a constant shear span ratio are carried out. Accordingly, the conclusions of this article are as follows:

1. From the test results, the shear strength of recycled concrete beams without web reinforcement has a size effect. In general, the shear strength is inversely proportional to the effective height of the section (h_0)—the smaller the h_0, the more obvious the size effect. In addition, the above-mentioned relationship can be better quantitatively described by the regression fitting formula.
2. Compared with the implicit finite element simulation results, the consistency between the explicit finite element simulation results and the experimental results is much higher. This situation not only shows that the damage constitutive model used in finite element modeling is reasonable, but it also shows that the explicit algorithm for solving this model is also reasonable.

This work will further promote the research of low-carbon-emission recycled concrete structures and the application of economic explicit finite element methods in static analysis of concrete structures.

Author Contributions: Conceptualization, W.W. and X.Z.; methodology, W.W. and X.Z.; software, X.Z.; formal analysis, W.W.; investigation, E.N.; resources, Y.-Q.G.; data curation, E.N.; writing—original draft preparation, X.Z.; writing—review and editing, W.W. and X.Z.; visualization, X.Z.; supervision, S.-Q.C. and Q.-W.Y.; project administration, Y.-Q.G.; funding acquisition, Y.-Q.G. All authors have read and agreed to the published version of the manuscript.

Funding: This research was funded by Natural Science Foundation of Zhejiang Province (LY20E080012).

Institutional Review Board Statement: Not applicable.

Informed Consent Statement: Not applicable.

Data Availability Statement: Not applicable.

Conflicts of Interest: The authors declare no conflict of interest.

References

1. Buck, A.D. Recycled Concrete as a Source of Aggregate. *ACI Struct. J.* **1977**, *74*, 212–219.
2. Safiuddin, M.D.; Alengaram, U.J.; Rahman, M.M.; Salam, M.M.; Jumaat, M.Z. Use of recycled concrete aggregate in concrete: A review. *J. Civ. Eng. Manag.* **2013**, *19*, 796–810. [CrossRef]
3. Jia, F. What is the low carbon economy. *Qiu. Shi.* **2009**, *19*, 50.
4. Livesley, R.K. The Finite Element Method in Structural and Continuum Mechanics. *Aeronaut. J.* **1967**, *71*, 659. [CrossRef]
5. Ma, Z.; Tang, Q.; Wu, H.; Xu, J.; Liang, C. Mechanical properties and water absorption of cement composites with various fineness and contents of waste brick powder from C&D waste. *Cem. Concr. Compos.* **2020**, *114*, 37–58.
6. Liang, C.; Pan, B.; Ma, Z.; He, Z.; Duan, Z. Utilization of CO_2 curing to enhance the properties of recycled aggregate and prepared concrete: A review. *Cem. Concr. Compos.* **2019**, *105*, 34–46. [CrossRef]
7. Brito, J.D.; Ferreira, J.; Pacheco, J.; Soares, D.; Guerreiro, M. Structal, material, mechanical and durability properties and behaviour of recycled aggregates concrete. *J. Build. Eng.* **2016**, *6*, 1–16. [CrossRef]
8. Bravo, M. Shrinkage and creep performance of concrete with recycled aggregates from CDW plants. *Mag. Concr. Res.* **2017**, *34*, 974–995. [CrossRef]
9. Zhu, Y.; Gao, G.; Xiao, J. Bending Performance Testing of Recycled Concrete Composite Slabs. *Concr. Cem. Produ.* **2012**, *06*, 49–52.
10. Cao, W.; Zhang, J.; Dong, H.; Qiao, Q.; Zhou, Z. Experimental study on bending behavior of middle strength recycled concrete floor slab. *J. Nat. Disasters* **2015**, *3*, 112–119.
11. Cheng, Z.; Ke, X.; Cheng, Y. Deformation Behavior and Bearing Capacity Calculation of Recycled Concrete Columns Constrained by Steel Tubular Tube. *J. Appl. Mech.* **2014**, *31*, 959–964.
12. Zhou, H.; Lin, Q.; Shu, Y. The Finite Element Analysis of Waste Fiber Recycled Concrete Column Compression Performance. *Appl. Mech. Mat.* **2015**, *3759*, 269–272. [CrossRef]
13. Ma, H.; Xue, J.; Liu, Y.; Zhang, X. Cyclic loading tests and shear strength of steel reinforced recycled concrete short columns. *Eng. Struct.* **2015**, *92*, 55–68. [CrossRef]
14. Barbara, S.B.; Danuta, B.H.; Małgorzata, S. Influence of Recycled High-Performance Aggregate on Deformation and Load-Carrying Capacity of Reinforced Concrete Beams. *Materials* **2020**, *13*, 186–207.
15. Li, S.; Zhang, Y.; Chen, W. Bending performance of unbonded prestressed basalt fiber recycled concrete beams. *Eng. Struct.* **2020**, *221*, 09–37. [CrossRef]
16. Xiao, J.; Lan, Y. Experimental Study on Shear Behavior of Recycled Concrete Beams. *Struct. Eng.* **2004**, *6*, 54–58.

17. Ayman, A.; Mohammad, A.; Mohammad, A.H. Predicting the contribution of recycled aggregate concrete to the shear capacity of beams without transverse reinforcement using artificial neural networks. *Case Stud. Constr. Mater.* **2020**, *13*, 1–13.
18. Yong, Y.; Zhao, X.; Xu, J.; Zhang, J. Machine Learning-Based Evaluation of Shear Capacity of Recycled Aggregate Concrete Beams. *J. Civ. Eng. Manag.* **2020**, *13*, 45–52.
19. Yan, G.; Sun, H.; Zhang, X.; Zhou, Y. Re-analysis of shear bearing capacity formula of recycled concrete beams. *Concrete* **2019**, *7*, 37–40.
20. Mahmoud, F.A.; Boissiere, R.; Mercier, C.; Khelil, A. Shear behavior of reinforced concrete beams made from recycled coarse and fine aggregates. *Structures* **2020**, *25*, 660–669. [CrossRef]
21. Su, T.; Wu, J.; Yang, G.; Jing, X.; Mueller, A. Shear Behavior of Recycled Coarse Aggregate Concrete Beams after Freezing-and-Thawing Cycles. *ACI Struct. J.* **2019**, *116*, 67–76. [CrossRef]
22. Zhao, J.; Yang, Q.; Zhang, Y.; Wang, X.; Lu, C.; Liang, C.; Sun, B. Experimental study on shear performance of recycled concrete beam without reinforcements. *Concrete* **2018**, *6*, 39–42.
23. Cheng, W.; Wang, T. *Concrete Structure: Design Principle of Concrete Structure*, 4th ed.; Wuhan University of Technology Press: Wuhan, China, 2008; pp. 71–104.
24. Gu, X. *Basic Principles of Concrete Structure*, 1st ed.; Tongji University Press: Shanghai, China, 2004; pp. 27–28, 55–80.
25. Bazant, Z.P. Size effect. *Int. J. Solids Struct.* **2000**, *37*, 69–80. [CrossRef]
26. Kani, G. How Safe are Our Large Reinforced Concrete Beams? *ACI Struct. J.* **1967**, *64*, 128–141.
27. Wu, W.K.; Thomas, T.C.; Shyh, J.H. Shear Strength of Reinforced Concrete Beams. *ACI Struct. J.* **2014**, *111*, 809–818.
28. Collins, M.P.; Kuchma, D. How safe are our large, lightly reinforced concrete beams, slabs, and footings. *ACI Struct. J.* **1999**, *96*, 482–490.
29. Bazant, Z.P.; YU, Q. Designing against size effect on shear strength of reinforced concrete beams without Stirrups:I. formulation. *J. Struct. Eng.* **2005**, *131*, 1877–1885. [CrossRef]
30. Bae, Y.H.; Lee, J.H.; Yoon, Y.S. Prediction of shear strength in high-strength concrete beams considering size effect. *Mag. Concr. Res.* **2006**, *58*, 193–200. [CrossRef]
31. Angelakos, D.; Bentz, E.C.; Collins, M.P. Effect of concrete strength and minimum stirrups on shear strength of large members. *ACI Struct. J.* **2001**, *98*, 290–299.
32. Zienkiewicz, O.C.; Taylor, R.L. *The Finite Element Method: Its Basis and Fundamentals*, 6th ed.; Beijing World Publishing Corporation: Beijing, China, 2008; pp. 15–20, 46–47.
33. Lv, X.; Jin, G. *Nonlinear Finite Element Theory and Application of Reinforced Concrete Structure*, 1st ed.; Chapter 1: Introduction; Tongji University Press: Shanghai, China, 1997; pp. 1–6.
34. Jiang, J.; Lu, X. *Finite Element Analysis of Concrete Structure*, 1st ed.; Chapter 1: Introduction, Chapter 4: The Constitutive Relationship of Concrete Materials; Tsinghua University Press: Beijing, China, 2005; pp. 1–5, 86–100.
35. Tartaglia, R.; Aniello, M.D.; Zimbru, M. Experimental and numerical study on the T -Stub behaviour with preloaded bolts under large deformations. *Structures* **2020**, *27*, 2137–2155. [CrossRef]
36. Ascher, U.M.; Ruuth, S.J.; Spiteri, R.J. Implicit-Explicit Runge-Kutta Methods for Time-Dependent Partial Differential Equations. *Appl. Numer. Math.* **1997**, *25*, 151–167. [CrossRef]
37. Choi, S.; Shah, S.P.; Thienel, K.C. Strain softening of concrete in compression under different end constraints. *Mag. Concr. Res.* **1996**, *48*, 103–115. [CrossRef]
38. Krajcinovic, D.; Fanella, D. A micromechanical damage model for concrete. *Eng. Fract. Mech.* **1986**, *25*, 585–596. [CrossRef]
39. Sabet, F.A.; Koric, S.; Idkaidek, A.; Jasiuk, I. High-Performance Computing Comparison of Implicit and Explicit Nonlinear Finite Element Simulations of Trabecular Bone. *Comput. Meth. Progr. Biomed.* **2020**, *200*, 105870. [CrossRef] [PubMed]
40. Khan, S.H.; Yildirim, I.; Ozdemir, M. Convergence of an implicit algorithm for two families of nonexpansive mappings. *Comput. Math. Appl.* **2010**, *59*, 3084–3091. [CrossRef]
41. Khennane, A. Performance design of reinforced concrete slabs using commercial finite element software. *Struct. Concr.* **2005**, *6*, 141–147. [CrossRef]
42. Harewood, F.J.; McHugh, P.E. Comparison of the implicit and explicit finite element methods using crystal plasticity. *Comput. Mater. Sci.* **2006**, *39*, 141–161. [CrossRef]
43. Oliver, J.; Huespe, A.E.; Cante, J.C. An implicit/explicit integration scheme to increase computability of non-linear material and contact/friction problems. *Comput. Meth. Appl. Mech. Eng.* **2008**, *197*, 1865–1889. [CrossRef]
44. Ted, B.; Jerry, L. Explicit algorithms for the nonlinear dynamics of shells. *Comput. Meth. Appl. Mech. Eng.* **1984**, *42*, 225–251.
45. Natário, P.; Silvestre, N.; Camotim, D. Web crippling failure using quasi-static FE models. *Thin-Walled Struct.* **2014**, *84*, 34–49. [CrossRef]
46. Yao, R.; Yi, G.; Li, X.; Zhang, W.; Wu, J. Simulation of failure process of reinforced concrete columns with extended finite element method. *Appl. Mech.* **2018**, *35*, 609–615.
47. Yu, D.; Yi, W. Experimental study on shear capacity of reinforced concrete cantilever beams with variable cross-sections without web reinforcement. *Build. Struct.* **2018**, *48*, 7–13.
48. Chen, H.; Yan, D. *Concrete Construction*, 2nd ed.; China Building Industry Press: Beijing, China, 1998; pp. 15–20.
49. Wang, L. *Elastic Theory*, 1st ed.; Science Press: Beijing, China, 1978; pp. 75–78, 119–121.
50. Lee, J.; Fenves, G.L. Plastic-damage model for cyclic loading of concrete structures. *J. Eng. Mech.* **1998**, *124*, 892–900. [CrossRef]

51. *Abaqus 6. 14 Theory Guide*; Dassault Systems Simulia Corp: Providence, RI, USA, 2014.
52. *Abaqus 6. 14 Analysis User's Guide (Volume III)*; Dassault Systems simulia Corp: Providence, RI, USA, 2014.
53. Chen, Z.; Xu, J.; Zheng, H.; Su, Y.; Xue, J.; Li, J. Basic mechanical properties test and stress-strain constitutive relation of recycled concrete. *J. Build. Mater.* **2013**, *1*, 28–36.
54. Guo, Z. *Strength and Deformation of Concrete: Experimental Foundation and Relations*, 1st ed.; Tsinghua University Press: Beijing, China, 1997; pp. 74–79.
55. Zhang, Q.; Guo, Z. Investigation on shear and shear strain of concrete. *J. Build. Struct.* **1992**, *5*, 17–24.